ACS Catalysis

pubs.acs.org/acscatalysis

Research Article

Potential-Dependent Free Energy Relationship in Interpreting the Electrochemical Performance of CO_2 Reduction on Single Atom Catalysts

Hao Cao,[#] Zisheng Zhang,[#] Jie-Wei Chen, and Yang-Gang Wang*

Cite This: *ACS Catal.* 2022, 12, 6606−6617

Read Online

ACCESS | Metrics & More | Article Recommendations | Supporting Information

ABSTRACT: Acquiring the fundamental understanding of electrochemical processes occurring at the complex electrode−liquid interface is a grand challenge in catalysis. Herein, to gain theoretical insights into the experimentally observed potential-dependent activity and selectivity for the CO_2 reduction reaction (CO_2RR) on the popular single-iron-atom catalyst, we performed ab initio molecular dynamics (AIMD) simulation, constrained MD sampling, and thermodynamic integration to acquire the free energy profiles for the proton and electron transfer processes of CO_2 at different potentials. We have demonstrated that the adsorption of CO_2 is significantly coupled with the electron transfer from the substrate while the further protonation does not show distinct charge variation. This strongly suggests that CO_2 adsorption is potential-dependent and optimizing the electrode potential is vital to achieve the efficient activated adsorption of CO_2. We further identified a linear scaling relationship between the reaction free energy (ΔG) and the potential for key elementary steps of CO_2RR and HER, of which the slope is adsorbate-specific and not as simple as 1 eV per volt as suggested by the traditional computational hydrogen electrode (CHE) model. The derived scaling relationship can reproduce the experimental onset potential (U_{onset}) of CO_2RR, potential of the maximal CO_2-to-CO Faraday efficiency (FE_{CO}), and potential where $FE_{CO} = FE_{H2}$. This suggests that our state-of-the-art model could precisely interpret the activity and selectivity of CO_2RR/HER on the Fe-N_4-C catalyst under different electrode potentials. In general, our study not only provides an innovative insight into the theoretical explanation of the origin of the solvation effect from the perspective of charge transfer but also emphasizes the critical role of electrode potential in the theoretical consideration of catalytic activity, which offers a profound understanding of the electrochemical environment and bridges the gap between theoretical predictions and experimental results.

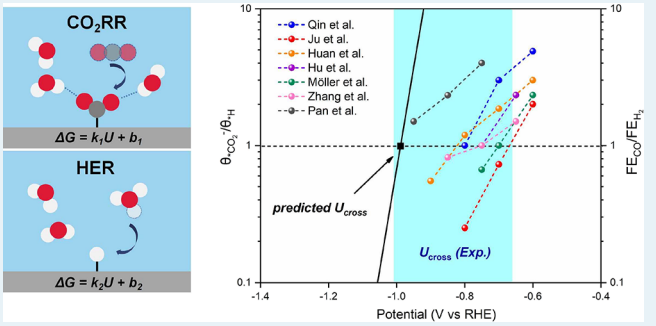

KEYWORDS: *ab initio molecular dynamics, thermodynamic integration, single-atom catalysis, CO_2 electroreduction, hydrogen evolution reaction, potential-dependent reaction free energy*

INTRODUCTION

Our increasing consumption of carbon-rich fossil fuels has inevitably resulted in significant emissions of green-house gases, most notably carbon dioxide (CO_2). The electrochemical CO_2 reduction (CO_2RR) has been recognized as an attractive technique for the reduction of the atmospheric concentration of CO_2 as well as the utilization of carbon resources.[1−4] Among the potential electrocatalysts in CO_2RR, the two-dimensional (2D) atomic dispersed transition metal catalysts in nitrogen-doped carbon (TM-N-C, TM = Fe,[5−7] Co,[8] Ni,[9−11] etc.) exhibit excellent performance for their lower overpotentials and high atomic efficiency compared to the traditional metal catalysts.[12−14] Extensive studies have been devoted to understanding the mechanistic nature of CO_2RR on this type of catalyst;[15−17] however, understanding the potential-dependent selectivity has remained challenging due to difficulty in properly addressing the complexity of the electrochemical interface.[18,19]

Density functional theory (DFT) calculation has been widely used to explore the electrochemical properties for CO_2RR on various catalysts.[20−22] By using the simple but effective computational hydrogen electrode (CHE) model,[23] previous studies have suggested that the CO_2 reduction to CO on TM-N-C catalysts involves two electron-proton transfer steps and the rate-determining step (RDS) is deemed as the first step (* + CO_2 + e^- + H^+ → *COOH), where the proton transfer (PT) step and electron transfer (ET) step were usually assumed to be

Received: March 25, 2022
Revised: April 14, 2022

https://doi.org/10.1021/acscatal.2c01470
ACS Catal. 2022, 12, 6606−6617

coupled in theoretical models.[24−26] However, Koper et al. pointed out that the mechanisms of CO_2 hydrogenation to the *COOH intermediate are diverse for different electrocatalysts, where the PT step and ET step could be sequential as in molecular electrocatalysts besides the coupled or concerted cases.[27−30] In the case of heterogeneous TM-N-C catalysts, experimental evidence has demonstrated that the CO formation rate on the Fe-N-C catalyst is independent of the pH value on the NHE scale, implying that the PT may not be the rate-determining step (RDS).[31] These pieces of evidence signify that the hydrogenation of CO_2 to *COOH probably need to be considered by decoupling the electron−proton transfer. However, in the usual practice, both overpotential (thermodynamics) and barriers (kinetics) are assumed to depend on the free energy change of the reaction intermediate before and after a coupled PCET.[32,33] Consequently, this may not be able to give an accurate estimation of either overpotential (associated with a non-coupled ET step) or selectivity (activation barriers to form different products). For example, many reported efficient FeN_x-based single-atom catalysts for CO_2 conversion to CO have low overpotential (less than ∼0.2 V) with the measured onset potential (U_{onset}) at −0.2 to −0.3 V *vs* RHE, whereas their DFT calculations suggested that the theoretically estimated overpotential for CO formation are mostly larger than 0.50 V (i.e., the ΔG of *COOH formation).[34−36] Similarly, this discrepancy is universal in studies of other TM-N-C catalysts (TM = Zn,[37] Co,[38] Ni,[10] etc.) due to the inability to quantitatively capture the potential-dependent free energy profile from overlooking the influences of the ET−PT decoupling, inconsistent work function of the catalyst surface along the reaction coordinate, and the role of the explicit water environment.[39−42]

Another challenge is to unify the hydrogen evolution reaction (HER) and CO_2RR kinetics under the same theoretical framework. Since a potential significantly more negative than 0 V RHE is required in a practical CO_2RR electrolyzer, the competing HER could significantly limit the Faradaic efficiency (FE) and production rate of CO and result in low selectivity.[43−45] As an unwanted phenomenon at low overpotential, protons (from hydronium in acidic media or water in alkaline media) would readily occupy the adsorption site and consume electrons supplied from the cathode, resulting in a side reaction with high FE_{H2}. It is reported that the measured FE_{H2} rapidly rises at −0.55 V *vs* RHE for Fe-N-C, while the corresponding electrode potential is about −0.70 V *vs* RHE for Ni-N-C.[46] However, the potential dependence of the competition between HER and CO_2RR pathways could not be quantified in the CHE-based simulation. To the best of our knowledge, there is still a lack of theoretical insight that could quantitatively match and well explain the experimental potential-dependent activity on TM-N-C catalysts.

In addition, the solvation stabilization on different intermediates can vary hugely due to their diverse chemical nature and dipole and hydrophilicity. Moreover, since the free energy is needed for the initial, transition, and final state of a reaction step, a sufficiently thick explicit water slab is necessary to ensure proper solvation of every species involved. To address this issue, ab initio molecular dynamics (AIMD) simulation has been successfully applied to study the catalytic reactions in electrochemical environments, for it could provide the dynamic properties of an electrolyte−solution interface at the quantum mechanical (QM) level.[47−50] However, the vast configurational space of a thick explicit water slab at an electrified surface needs very efficient and consistent sampling along the reaction coordinate; otherwise, the resulting reaction free energy would be biased toward a few selected local minima configurations.

In this study, we first explored the free energy profile for the decoupled electro−proton transfer of *COOH intermediate formation from CO_2 by employing DFT-based constrained AIMD simulation combined with the thermodynamic integration (TI) method and fully explicit solvation of 20 Å thickness. Potential-dependent reaction free energy profiles are obtained by introducing counterions (Na^+, Cl^-) to tune the work function of the system. An ET−PT decoupled and H bond-assisted mechanism of CO_2 activation is revealed based on the potential-dependent reaction profile and molecular fragment calculations. Linear potential-dependent free energy relationships of CO_2 activation and *H formation (for the HER side reaction) are found, based on which we predicted the onset potential (U_{onset}) of CO_2RR, the potential of the maximum FE_{CO}, and the potential of the FE_{CO}−FE_{H2} crossover in good agreement with experimental reports.

METHODS

Model Setup for the Electrocatalytic Interface. The Fe-N_4-C substrate was modeled by a single layer of four nitrogen atom-doped graphene with a single Fe atom embedded in the center (Figure S1). The Fe-N_4-C slab was composed of a 6 × 4 supercell with dimensions of 17.04 × 14.76 × 20.00 $Å^3$ and was allowed to repeat periodically. The empty spaces of the simulation box were filled with bulk water, which contained 141 H_2O molecules and possessed an average density of ∼1 g/cm^3. The radial distribution functions (RDFs) and the coordination number (from integration of the RDFs) of O−O and O−H for validation of the liquid water structure are also provided in Figure S1, which is consistent with experimentally determined results,[51] validating the proper convergence of the water structure to bulk behaviors. This model gives consistent coordination number with experimental characterizations[52−54] and has been used in many recent theoretical studies.[50,55]

DFT Method Details. All Born−Oppenheimer molecular dynamics (BOMD) simulations and constrained MD simulations were performed by employing the CP2K/Quickstep package.[56] The electronic structure calculations are described by DFT with the spin-polarized Perdew−Burke−Ernzerhof (PBE) functional and mixed double-ζ Gaussian and plane-wave (GPW) basis sets with an energy cutoff of 400 Ry.[57] The core electrons were modeled by Goedecker−Teter−Hutter (GTH) pseudopotentials with 16, 4, 5, 6, and 1 valence electrons for Fe, C, N, O, and H, respectively. The MD simulations were sampled by the canonical (NVT) ensemble employing Nose−Hoover thermostats with a time step of 1.0 fs at the target temperature of 300 K.[58,59] In all the calculations, the DFT-D3 method proposed by Grimme et al. was adopted to better describe the noncovalent interactions.[60,61]

Free Energy Calculation. In the thermodynamic integration (TI) method, the reaction free energy and kinetic barrier are obtained by applying a holonomic constraint on the reaction coordinate (ζ) during MD simulations and integrating over the average unbiased force associated with the reaction coordinate,[62,63] as shown in eq 1

$$\Delta A(\zeta_a, \zeta_b) = -\int_{\zeta_a}^{\zeta_b} F(\zeta) d\zeta \quad (1)$$

where $\Delta A(\zeta_a, \zeta_b)$ is the free energy difference between two reaction coordinates (ζ_a and ζ_b) and $F(\zeta)$ is the averaged

https://doi.org/10.1021/acscatal.2c01470
ACS Catal. 2022, 12, 6606−6617

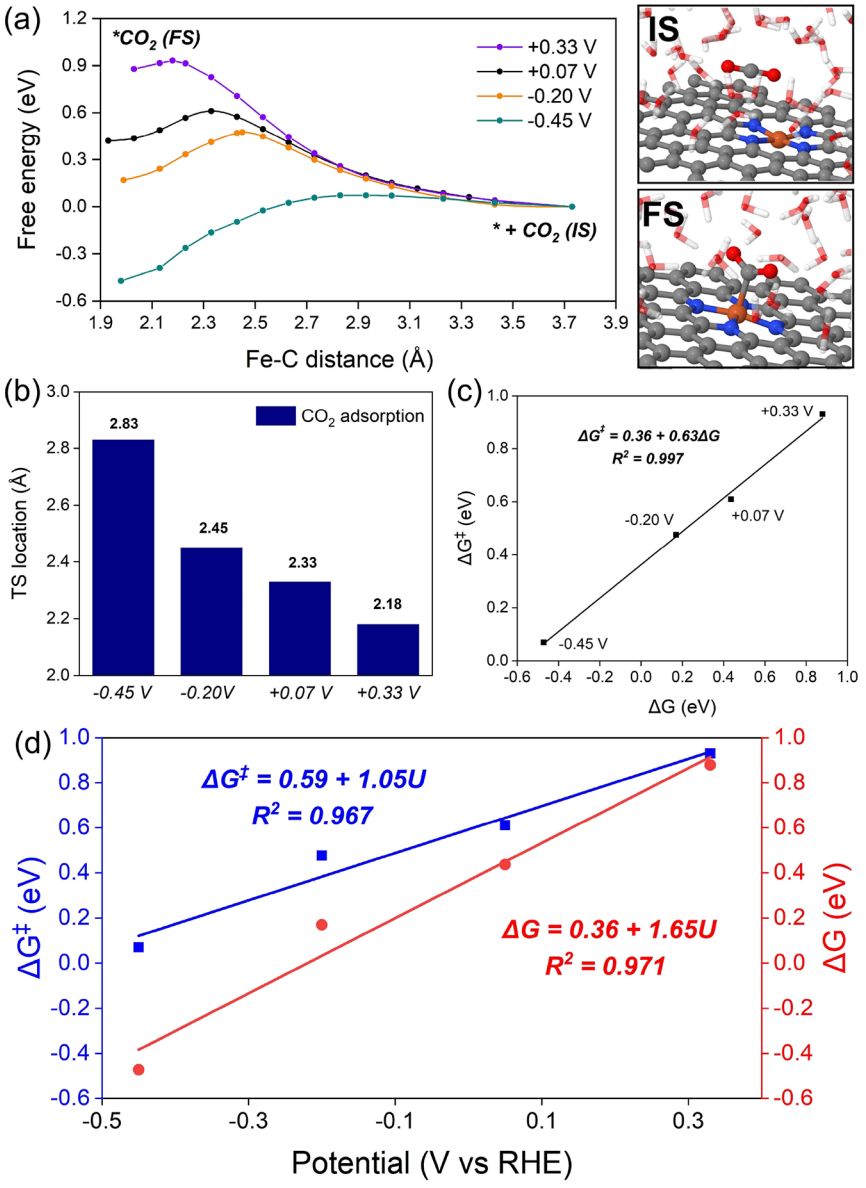

Figure 1. Potential-dependent free energetics of CO_2 adsorption at the Fe-N_4-C/water interface. (a) Free energy profiles of CO_2 adsorption at +0.33, +0.07, −0.20, and −0.45 V *vs* RHE. (b) Location of transition states (TS) during adsorption at different potentials. The fitting linear relationship between (c) ΔG and $\Delta G^{\ddagger}$ and (d) $\Delta G/\Delta G^{\ddagger}$ and potential.

constrained force. For CO_2 adsorption on the single Fe site ($CO_2 + e^- + * \rightarrow *CO_2^-$), the distance between Fe and C atoms is chosen as the collective variable (CV), which is defined by eq 2

$$\mathrm{CV} = \zeta(\mathrm{r}) = |\mathrm{r_{Fe}} - \mathrm{r_C}| \tag{2}$$

where r_{Fe} and r_C refer to the coordinates of the Fe atom and the C atom of CO_2 (Figure S3a).

For the protonation of $*CO_2^-$ under acidic conditions ($*CO_2^- + H_3O^+ \rightleftarrows *COOH + H_2O$), the CV is defined by eq 3

$$\mathrm{CV} = \zeta(\mathrm{r}) = |\mathrm{r_{OA}} - \mathrm{r_H}| - |\mathrm{r_{OB}} - \mathrm{r_H}| \tag{3}$$

where r_{OA} refers to the coordinate of the O atom on the hydronium ion (H_3O^+), r_{OB} refers to the coordinate O atom of the adsorbed CO_2, and r_H refers to the coordinate of the solvated proton on H_3O^+ (Figure S3b).

For the solvated proton (H_3O^+) adsorption on the single Fe site under acidic conditions ($H_3O^+ + e^- + * \rightarrow *H + H_2O$), the CV is defined by eq 4

$$\mathrm{CV} = \zeta(\mathrm{r}) = |\mathrm{r_{Fe}} - \mathrm{r_H}| - |\mathrm{r_O} - \mathrm{r_H}| \tag{4}$$

where r_{Fe} refers to the coordinate of the Fe atom, r_O refers to the coordinate of the O atom on H_3O^+, and r_H refers to the coordinate of the solvated proton on H_3O^+ (Figure S3c).

Note that the free energy profile with this method (TI on finite-temperature constrained AIMD trajectories, with fully explicit solvation) can properly incorporate the entropy contribution and the solvation effect when the sampling is sufficient; hence, it is not needed to use special thermochemical corrections such as the gas-phase correction for static gas-phase or implicit solvation DFT calculations.[64]

Modeling the Influence of Applied Potential. The potential of zero charge (PZC) is a crucial concept in the field of electrochemistry, which can be experimentally confirmed by the measurement and regulation of surface net charge. In this case, the theoretical adjustment of the surface electrode potential is applied by adding alkali metal ions (K^+, Na^+) or halide ions (F^-,

https://doi.org/10.1021/acscatal.2c01470
ACS Catal. 2022, 12, 6606−6617

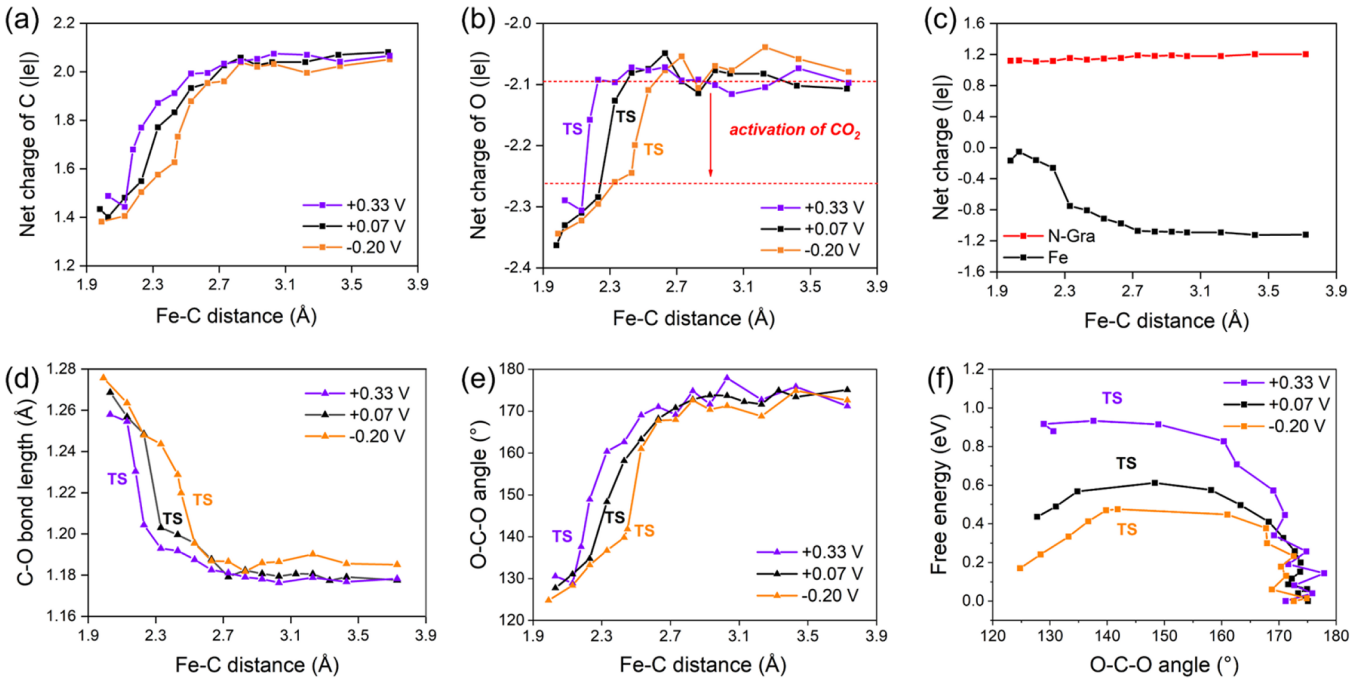

Figure 2. Exploring the mechanistic nature of CO_2 activation on the Fe active site. (a) Evolution of Bader charge on (a) C, (b) O, and (c) Fe along the Fe−C distance coordinate at different potentials. Evolution of (d) the C−O bond length and (e) O−C−O angle along the Fe−C distance coordinate. (f) Free energy profile of CO chemisorption with the O−C−O angle being the reaction coordinate. Results obtained at potentials of +0.33, +0.07, and −0.20 V *vs* RHE are shown.

Cl^-, etc.) into the liquid layer to increase or reduce the net charge on the surface. In our study, different amounts of Na^+ and Cl^- were added to the liquid model (Figure S2) and AIMD simulations were further performed to equilibrate the system. The electrode potentials (Φ) of the TM-N_4-C surface were then determined by eq 5

$$\Phi = \frac{\sigma}{C} + \Phi_{PZC} \tag{5}$$

where σ is the calculated surface net charge via Bader charge analysis[65] and C and Φ_{PZC} are the experimental capacitance of pristine graphene (~21 $\mu F/cm^2$) and potential of zero charge (−0.07 V *vs* RHE), respectively.[66,67] We considered the average value of the potential at the initial state (U_{IS}) and (U_{FS}) as the potential (U_r) of the reaction (i.e., $U_r = (U_{IS} + U_{FS})/2$). Note that here, the added cations/anions serve no chemical role, and this technique has been shown to properly describe the potential dependence of electrochemical barriers.[68] The detailed electrode potentials, surface charges, and corresponding correction terms for each free energy profiles are provided in Table S1.

Pros and Cons of the Constant-Charge AIMD-TI Approach *vs* Constant-Potential Methods. Here, we briefly comment on the challenges in obtaining the electrochemical free energy profile with AIMD simulations (for detailed discussion, see Supplementary Note S8). Obtaining an accurate free energy profile at constant potential, i.e., doing sufficiently sampling for both the configurational entropy and electronic contributions within the grand canonical ensemble (of electrons), has remained a challenging task. In this work, each constrained AIMD simulation is performed within the canonical ensemble with constant charge, which inevitably comes with a shift in the work function along the reaction coordinate. However, the influence of such a shift on the reaction free energy is found to be minimal (Table S1) and does not affect any of the major conclusions of this work. Another approach, the constant-potential method, addresses the system as a grand canonical ensemble of electrons and equilibrates the system with an electron reservoir of a certain work function (theoretical potentiostat). This approach provides exact constant-potential results; however, it also introduces some extra error and artifacts: (i) implicit solvation is usually required to screen the extra charge, which is known to cause unphysical solvation at the explicit/implicit interface and countercharge penetration problems (especially for 2D materials).[69] In principle, the sampling is accomplished by multiple short-time (usually ~10 fs) MD simulations, each within the canonical ensemble. This potentiostating could be too aggressive and fail to properly equilibrate the system at each number of electrons, causing biased configurational sampling (in the non-equilibrium region). Since we expect the configurational entropic contribution to the reaction free energy to play a key role, we run multiple constant-charge MDs within the canonical ensemble at different work function ranges to ensure proper equilibration and extensive sampling. This approach should yield more realistic solvation free energies and configurations while not compromising the accuracy too much from the potential-variation along the reaction coordinate.

Molecular Fragment Calculations. The molecular fragments are modeled using the Gaussian 16 program[70] (Revision C.01). The geometry optimizations and potential energy surface (PES) scans are performed using the PBE0 functional[71] with def2-TZVP basis sets[72] and D3 correction (Becke−Johnson damping)[61] to better account for the dispersion interactions. Molecular orbital analysis, Hirshfeld/AIM population analysis, and Mayer bond order analysis are performed using the Multiwfn program on the converged wavefunctions from DFT calculation.[73]

https://doi.org/10.1021/acscatal.2c01470
ACS Catal. 2022, 12, 6606−6617

RESULTS AND DISCUSSION

Potential-Dependent CO_2 Chemisorption. To understand how different applied potentials influence the most concerned initial electron−proton transfer step ($* + CO_2 + e^- + H^+ \rightarrow *COOH$) in CO_2RR on the Fe−N_4−C catalyst, we first construct the free energy profiles for CO_2 adsorption at different electrode potentials (Figure 1a) by TI on the equilibrated constrained AIMD trajectories. It is observed that the adsorption free energy (ΔG) is strongly dependent on the electrode potentials. Specifically, as the potential shifts negatively from +0.33 to −0.45 V, ΔG accordingly lowers from 0.88 to −0.47 eV. Similarly, the free energy barrier ($\Delta G^{\ddagger}$) dramatically decreases from 0.93 to 0.07 eV. This indicates that the low electrode potential can facilitate the CO_2 adsorption in both thermodynamics and kinetics.

Furthermore, the locations of transition states (TS) at different potentials are displayed in Figure 1b, where the difficulty of CO_2 activation can be judged by Fe−C distance, which corresponds to the reaction coordinate of the TS on the free energy profile. Under +0.33 V, the Fe−C distance at the TS is as short as 2.18 Å, indicating that the CO_2 molecule has to move very close to the catalyst surface for the full activation of CO_2. However, as the potential shifts to −0.45 V, the corresponding distance increases to 2.83 Å, indicating that the CO_2 can be activated at a further distance from Fe, which is likely due to a higher electron density at the catalyst surface at a high overpotential.

Interestingly, we found a strong linear Brønsted−Evans−Polanyi (BEP) relationship ($R^2 = 0.997$) between ΔG and $\Delta G^{\ddagger}$ (Figure 1c). Likewise, Figure 1d shows that both ΔG and $\Delta G^{\ddagger}$ correlate decently with the electrode potential, where the R^2 values are 0.969 and 0.962, respectively. Note that here, the intercept corresponds to the energetics at zero potential, while the slope quantifies the potential dependence of the reaction.

The potential-dependent free energy profile, the short Fe−C distance in the final state (FS), and the bending of CO_2 during the CO_2 adsorption suggest that it is a chemisorption process, which involves ET from the catalyst. To confirm this, we analyzed the Bader charge variation for the catalyst substrate and the CO_2 species along the reaction coordinate of CO_2 adsorption based on the constrained MD simulations in Figure 2. Unsurprisingly, both the net charges of C and O atoms show a significant decrease during the adsorption process. This confirms that the neutral linear CO_2 is reduced to the bent CO_2^- anion where the extra electron resides in the Π* orbital as characterized by the uniform negative shift of the Bader charge on C and O. However, the charge states of C and O differ in that the charge of the C atom gradually decreases from ∼2.08|e| to ∼1.43|e| as CO_2 approaches the surface, while the O atoms experience a rapid charge transfer, which takes place in a very short distance (Figure 2a,b). Prior to approaching the transition state (TS), the O atoms of CO_2 experience no obvious electron transfer and even show a slight positive charge increase. However, after crossing over the TS, the charge on the O atom undergoes a significant negative shift by ∼0.17|e|.

Having identified the change in the charge state of C and O, we further analyzed the charge variation of the catalyst substrate to understand the charge source for activating CO_2. As shown in Figure 2d, it is found that the net charge of the Fe atom shows a minor change (less than ∼0.1|e|) upon CO_2 adsorption at +0.07 V, while the charge on the substrate increases significantly (more than ∼0.9|e|). This contrast suggests that the charge transfer from the catalyst to CO_2 is mainly contributed by the charged N-doped graphene substrate (as an electron reservoir). The Fe center, however, undergoes negligible changes in the FeN_4 geometry (Figure S19) and remains in its initial charge state (II). It is worth noting that despite the charge state of Fe staying almost unchanged, we observed a change in the spin moment on the Fe center from 2 to 0 in the CO_2 activation process. This can be rationalized by the change in the coordination environment of the Fe center upon Fe−C formation: In the IS, Fe is strongly coordinated by four neighboring N atoms and weakly coordinated by a backside water, giving a square pyramidal crystal splitting (Figure S20a,). Since the electron configuration of Fe(II) is [Ar]$3d^6$, the d_{xz} and d_{yz} are doubly occupied, while the nearly degenerate d_{z2} and d_{xy} are singly occupied, leading to a high-spin triplet state. In the FS, the activated CO_2 coordinates to the Fe, resulting in an octahedral crystal field splitting where d_{xy}, d_{xz}, and d_{yz} become degenerate and doubly occupied, bringing the system back to a low-spin singlet (Figure S20c). These trends are also observed at −0.20 and +0.33 V (Figure S8).

The inconsistency between charge shifts on C and on O along the reaction coordinate is likely caused by the non-simultaneity of ET and the geometric bending of the $*CO_2$. It can be seen in the molecular orbital (MO) diagram (Figure S10) that the HOMO and LUMO of the linear CO_2 are the s−p σ^* ($5\sigma_g$) orbital and p−p π^* ($2\pi_u$) orbital, respectively. When an electron is supplied to reduce it vertically, the added electron goes into the C-centered s−p σ^* ($5\sigma_g$), causing a major charge shift by −0.539|e| on C (from +0.33 to −0.209|e|) and a minor shift by −0.230|e| on O (from −0.165 to −0.395|e|). The bond length of C−O only gets slightly elongated by 0.02 Å since the conjugate system is intact. However, when the CO_2^- adapts to the bent configuration, the energy level of the s−p σ^* ($5\sigma_g$) and p−p π^* ($2\pi_u$) switches, causing the crossover between the HOMO and LUMO. As a result, the unpaired electron in bent CO_2^- goes to the distorted p−p π^* ($6a_1$) orbital where the contribution from O is dominant. This induces a charge redistribution within the molecular fragments, shifting 0.202|e| from C to O. The filling of p−p π^* ($6a_1$) also lowers the Mayer bond order of each C−O by 0.49 and elongates the C−O by 0.08 Å compared to the IS (Table S2). This could explain the evolution of the C−O bond length along the free energy profile (Figure 2d) where the C−O bond length stays almost unchanged at around 1.19 Å in the IS−TS segment and then experiences a sudden jump from c.a. 1.20 to 1.27 Å in the TS−FS segment.

Having identified CO_2 bending to be a key process, we move on to investigating how the O−C−O angle changes along the reaction coordinate of the Fe−C distance. In Figure 2e, the O−C−O stays around 175° in the first half of the IS−TS segment. After crossing the position corresponding to an Fe−C distance of c.a. 2.7 Å, there comes a dramatic decrease in the O−C−O angle from c.a. 170° to 130°. Such a trend suggests that O−C−O is a better collective variable for describing the region around the TS on the free energy surface. Hence, we reconstructed the free energy surface (Figure 2f) by using the O−C−O angle as the CV for TI. Under this "bending coordinate", the first half of the IS−TS segment forms a "cliff" on the FES since the initial ET is vertical and causes no change in the configuration of CO_2. At about 170°, the bending process starts, and the FE profile ahead forms a smooth bump with a continuous landscape free of spikes or sudden jumps. In addition, the TS locations (relative to IS and FS along the reaction profile) at different potentials are about the same, c.a. 140°, which is in sharp contrast with the case in

https://doi.org/10.1021/acscatal.2c01470
ACS Catal. 2022, 12, 6606−6617

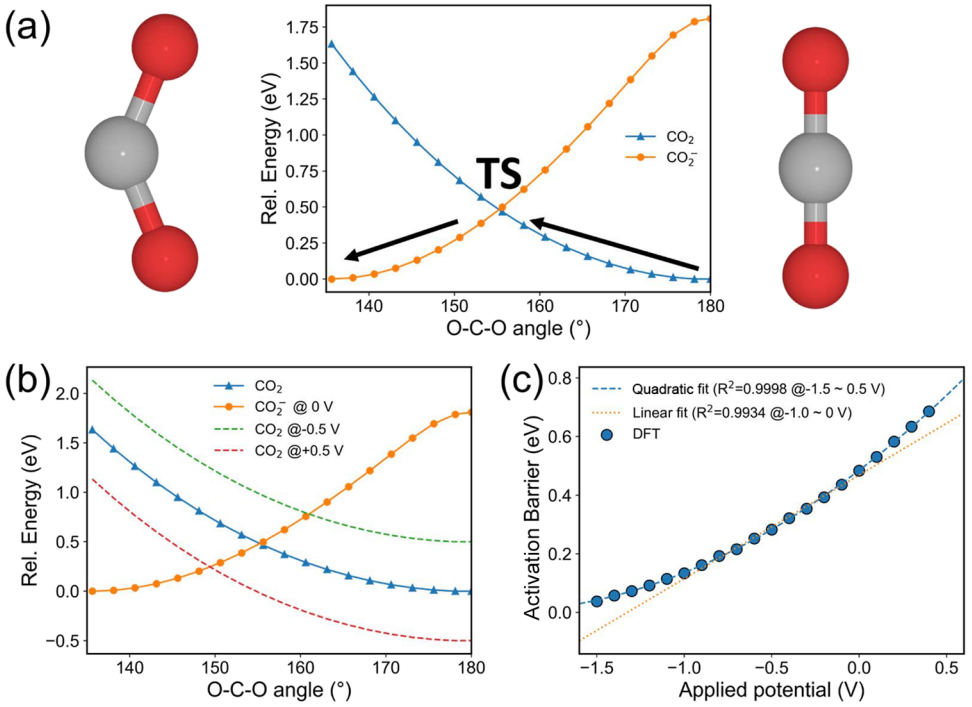

Figure 3. Potential energy surface (PES) of the CO_2 reduction. (a) PES scan of the neutral CO_2 and anionic CO_2^-, the energy values are referenced against the global minima configurations. (b) PES of CO_2 reduction at different potentials. (c) Relationship between the activation barrier and the applied potential (which is also $\Delta G/e$) for the CO_2 species. Two fitting methods are used, with their R^2 and applicable range provided in the legend. Linear BEP is broken in the high overpotential range due to inharmonicity of the PES of CO_2^-.

Figure 1a where the TS location exhibits a strong potential dependence.

From the discussions above, we could conclude on the mechanism of the CO_2 adsorption on Fe-N_4-C as the following: (i) At the IS, the linear, charge-neutral CO_2 is weakly physisorbed above the FeN_4 motif. (ii) In the first half of the IS−TS segment, CO_2 approaches the Fe center while maintaining its charge state and configuration. (iii) About the midpoint of the IS−TS segment (high overpotential would advance this event), the electrified catalyst surface initiates an ET to the C-centered s−p σ^* orbital in CO_2 *via* the Fe center. The CO_2 is reduced to CO_2^- near-vertically. (iv) In the second half of the IS−TS segment, the CO_2^- coordinates to the Fe center via C. The Fe−C formation also induces CO_2^- bending, which gradually raises the energy level of s−p σ^* (current HOMO) while lowering the energy level of p−p π^* (current LUMO). (v) At the TS, the s−p σ^* and p−p π^* become degenerate, and the unpaired electron starts to cross into the p−p π^* (current HOMO) and redistribute negative charge from C to O. (vi) In the TS−FS segment, crossover between s−p σ^* and p−p π^* takes place, reversing the LUMO and HOMO, and the unpaired electron completely crosses to p−p π^* (current HOMO) and weakens the C−O by 0.5 bond order. In this process, the catalyst surface keeps supplying electrons to the C through Fe−C to replenish the loss of electron density on C. (vii) At FS, the bending process ends and a bent $*CO_2^-$ is formed.

At the end of this section, we would like to comment on the origin of the linear relationship we obtained in Figure 1. In Figure 3, we show the PES of O−C−O bending of neutral CO_2 and anionic CO_2^- from relaxed scan. The PES of neutral CO_2 has only one extremum at 180°, while the PES anionic CO_2^- has a minimum at c.a. 135°. The crossing point of the two PESs is the TS of the CO_2 reduction process. Although the picture of facile ET during the adsorption process is indeed similar to the case of CO_2 activation on Au and Ag surfaces reported in ref 20, we intend to claim that the CO_2RR mechanisms on metal catalysts and single atom catalysts (TM-N-C) are not identical, since the latter features more discrete d energy levels (which resemble more the macrocyclic complexes) while the former has a continuous density of state around the Fermi level (metallic property).[15,39] By applying a positive or negative electrode potential, we are effectively shifting the PES of the initial state (neutral CO_2 + electron) downward or upward, respectively. Since the near-minimum regions of both PESs have a parabolic shape, treating both PESs as parabolas and analytically solving for the ΔG, $\Delta G^{\ddagger}$, and the TS location would yield a linear correlation between each of them, which is what we have known as the BEP relation. However, in the case of CO_2 reduction, the PES of anionic CO_2^- is not well approximated by a parabola due to the local minimum at 180° corresponding to the vertical reduction product of linear CO_2. Such inharmonicity and asymmetry between the PES of the reactant and product causes significant deviation of the potential dependence relation from linear behavior, especially at extreme positive or negative potentials (Figure 3c). Such a relationship could be better approximated by a quadratic function with an R^2 of 0.9998. However, quadratic regression could cause severe overfitting problems especially in the case of this study where the amount of data points (at different electrode potentials) is relatively small. Moreover, in the region corresponding to −1.0 to 0 V, the BEP relation is not significantly affected by the inharmonicity and a decent linear fitting with R^2 of 0.993 could be obtained. Therefore, we believe that the linear potential dependence of free energy change and barriers of the CO_2 activation process should hold in the potential window of +0.3 to −0.7 V *vs* RHE.

https://doi.org/10.1021/acscatal.2c01470
ACS Catal. 2022, 12, 6606−6617

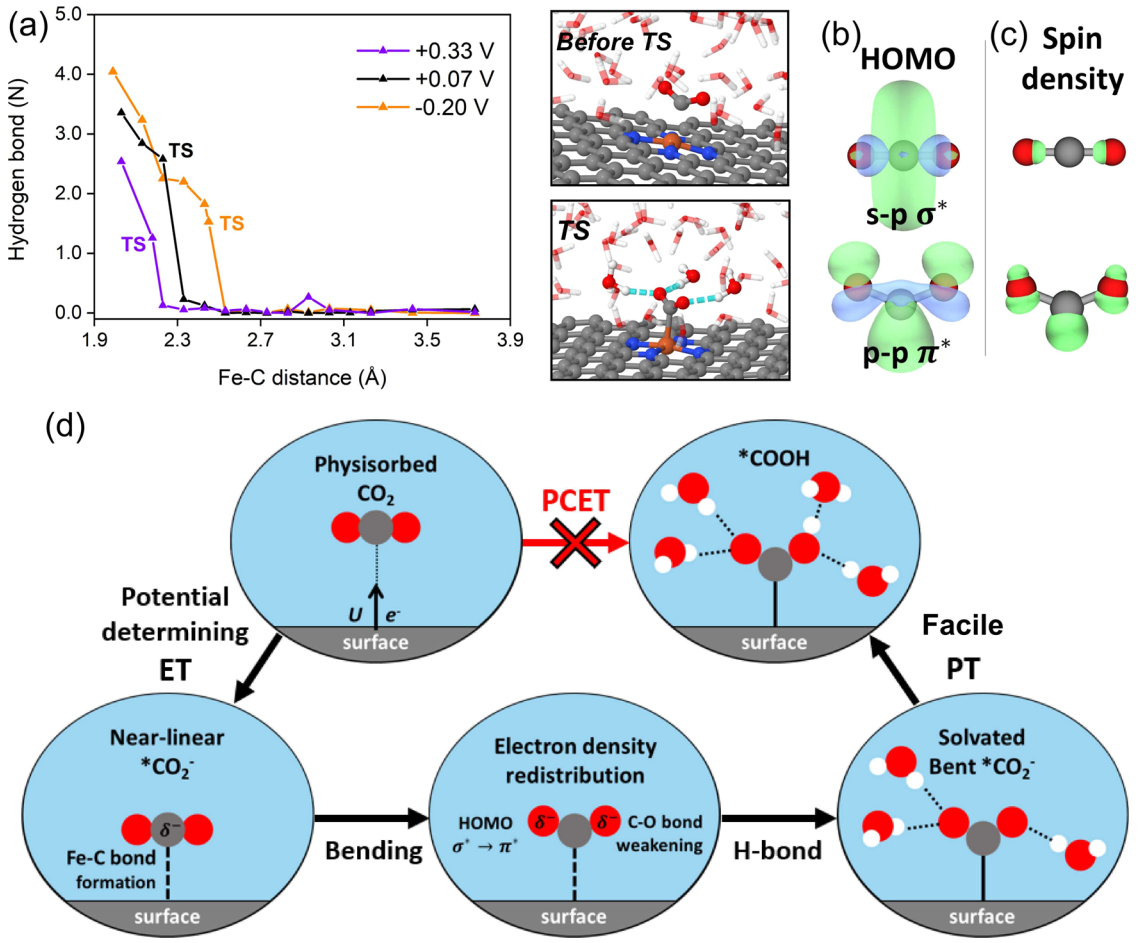

Figure 4. Solvation stabilization of the TS and a revised CO_2 activation mechanism. (a) Statistic number of hydrogen bonds between the solvation environment and CO_2 reactant at different potentials on Fe-N_4-C and snapshots of the solvation environment around CO_2 before the transition state (TS) and at TS. (b) HOMO and (c) spin density distribution of the CO_2^- anion in a linear or bent configuration. (d) Revised mechanism of the CO_2 chemisorption based on the potential-dependent free energy profile and chemical bonding analysis.

Evolution of Local Hydrogen Bond Structure during CO_2 Activation. The aqueous electrocatalytic CO_2RR on Fe-N_4-C occurs in a complex environment where the water molecules could interact strongly with adsorbates through the hydrogen bond (H-bond) interaction. To understand how such an effect evolved along the reaction coordinate, we counted the number of H-bonds between the oxygen atoms in CO_2 and surrounding water molecules during the ET step from constrained AIMD simulations, where the criteria of hydrogen bond formation between $*CO_2^-$ and the solvation environment are detailed in the Supporting Information. As shown in Figure 4a, the H-bonds between O in activated CO_2 and the nearby water molecules are rapidly formed once the TS is reached, which suggests that the CO_2 transforms to a state that strongly interacts with its water environment. Such transformation originates in the HOMO−LUMO crossover as discussed in the last section. To be specific, when the CO_2^- bends to the TS configuration, the HOMO of the molecular fragment shifts from a symmetric nonpolar s−p σ^* to a distorted, highly polar p−p π^* (Figure 4b). The crossover causes the spin density (contributed exclusively by the electron transferred from the catalyst) to redistribute to the terminal O atoms (Figure 4c), which as a result become strong H-bond acceptors.

Interestingly, as the potential shifts from +0.33 to −0.20 V, the reaction coordinate corresponding to the H-bond onset shifts accordingly as the position of TS shifts closer to the IS (Figure 4a). In other words, the H-bond interaction exerted on CO_2 strengthens at a more negative potential, which indicates that this solvation effect during the ET step is also potential-dependent, which is likely due to polarized contact water bilayers acting as stronger H-bond donors.

This can well explain why the total slope (k) of the G−U relationship is not as simple as 1 eV/V on CO_2 adsorption. Since the contribution of the potential-dependent solvation effect is actually included during constrained MD simulation, the reaction free energy derived by TI can be resolved into three parts, which is $\Delta G = \Delta G_{chem} + \Delta G_{ele} + \Delta G_{sol}$, where ΔG_{chem}, ΔG_{ele}, ΔG_{sol} are the chemical, electrostatic, and solvation contributions for the reaction free energy, respectively. It is noted that only the last two parts would be affected by the electrode potential. Therefore, the k can also be divided into two components, $k_{ele} + k_{sol}$, where k_{ele} is the charge transfer number and k_{sol} is the solvation effect coefficient. k_{ele} is calculated as ∼1 eV/V from Bader charge analysis (Table S1), and thus k_{sol} is about 0.65 eV/V in this case.

Similar trends in H-bond formation are also observed on Co-N_4-C (Figure S13) despite the very different free energetics of the CO_2 activation (Figure S9). Hence, we believe the potential-dependent solvation stabilization of activated CO_2^- to be a universal effect in CO_2RR on other similar TM-N-C (TM = Co,

https://doi.org/10.1021/acscatal.2c01470
ACS Catal. 2022, 12, 6606−6617

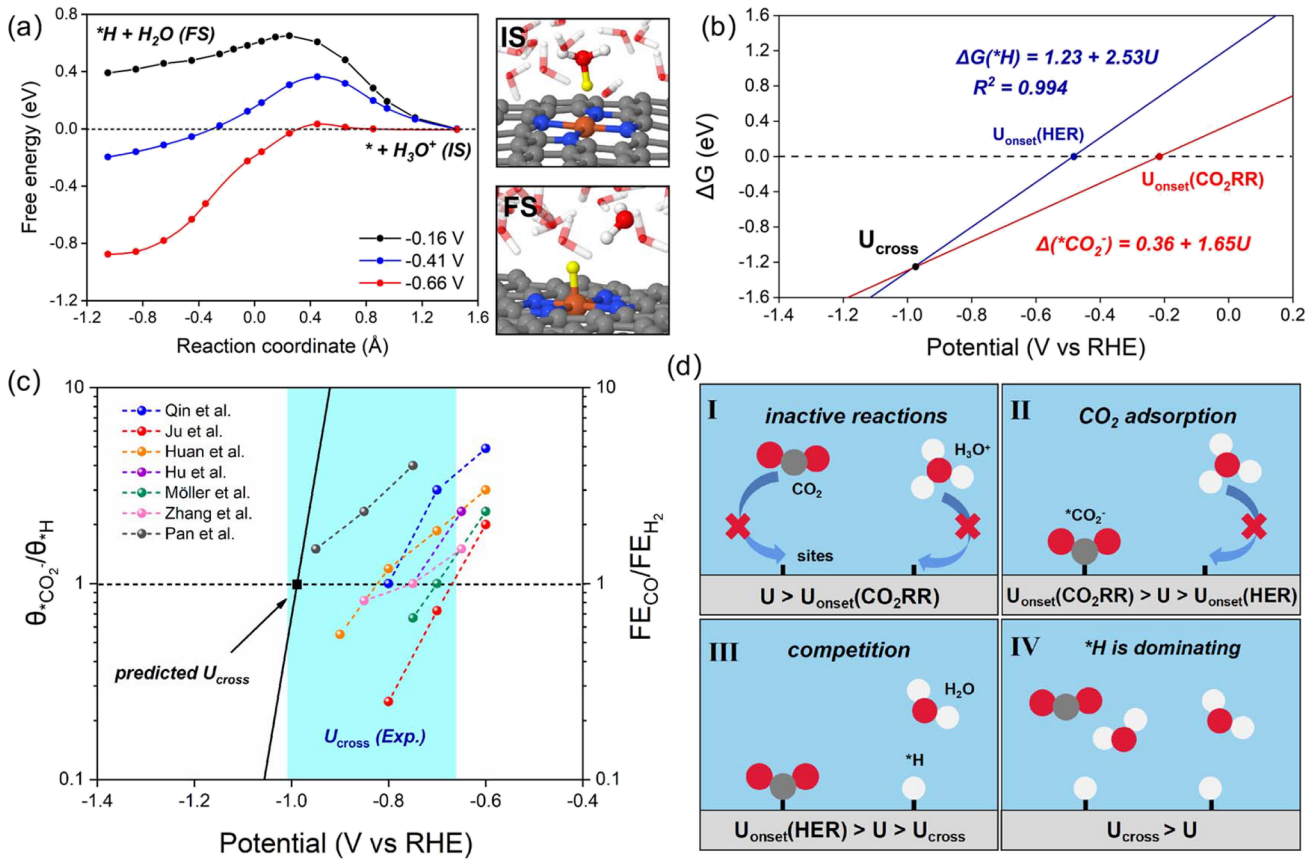

Figure 5. (a) Free energy profile of solvated proton adsorption at −0.16, −0.41, and −0.66 V *vs* RHE. (b) Fitting linear relationship (ΔG–U) between $\Delta G(*CO_2^-)$, $\Delta G(*H)$, and potential. The U_{onset}(HER), U_{onset}(CO_2RR), and U_{cross} correspond to the potentials at $\Delta G(*CO_2^-) = 0$, $\Delta G(*H) = 0$, and $\Delta G(*CO_2^-) = \Delta G(*H)$, respectively. (c) Comparison of theoretical U_{cross} and experimental U_{cross}. The solid black line is the relationship between $\theta_{*CO2-}/\theta_{*H}$ and potential, and the dotted lines are the relationships between experimental FE_{CO}/FE_{H2} and potential from previous studies.[34−36,38,46,53,78] The theoretical U_{cross} is the potential at $\theta_{*CO2^-} = \theta_{*H}$, and the experimental U_{cross} is the potential at $FE_{CO} = FE_{H2}$. (d) Illustration of CO_2RR activity and selectivity at different potentials.

Ni, etc.) systems, independent from the nature of the metal center.

We would like to emphasize that, due to the strong solvation effect and its dynamic nature, explicit solvation is a must even for a qualitatively correct description of the FES of CO_2 activation. In fact, the chemisorbed CO_2 configuration could not be obtained at all on Fe-N_4-C using simple slab-vacuum or implicit solvation models since the highly polar FS is not sufficiently stabilized without the directional and dynamic H-bond interactions with a sufficient explicit liquid water environment. To address the vast configurational space of solvation configurations, efficient and unbiased sampling is required; otherwise, the configurational entropy contribution to the reaction free energy would be inaccurate.

Facile Proton-Transfer Step. The above results suggest that the CO_2 adsorption is in fact coupled with the electron transfer. As the electrode potential negatively shifts, the TS and FS can be increasingly stabilized by the polarized water environment via H-bonds at the electrified electrode−water interface, making the CO_2 activation process both kinetically and thermodynamically favorable. However, we are not observing the spontaneous formation of the *COOH intermediate in this activation process, which could be attributed to the stronger acidity of carboxylic acid compared to that of neutral water. Therefore, we further performed constrained MD and thermodynamic integration methods to explore the protonation of $*CO_2^-$ by an explicit hydronium, i.e., $*CO_2^- + H_3O^+ \rightarrow *COOH + H_2O$. Figure S15 shows the calculated free energy profiles of the reaction at different electrode potentials. It is shown that with the potential decreasing from +0.33 to −0.19 V, the reaction free energy (ΔG(PT)) only slightly shifts from 0.14 to 0.26 eV and the process is almost barrierless. This indicates that the proton uptake from the adjacent hydronium ion is much more facile compared to CO_2 adsorption, which is consistent with the experimentally observed weak pH dependence of CO_2RR.[31,74] Moreover, the slope of the linear relation between ΔG(PT) and potential is only −0.20 eV/V (Figure S15b), suggesting that the level of electrode potential has less impact on the PT step compared with the ET step. As a result, compared to the strongly potential-dependent ET step, the PT step is probably less decisive in determining the CO_2RR activity. Additionally, the net charges of the Fe adsorption site are also nearly unchanged during PT (Figure S16), implying that the Fe would similarly maintain its oxidation state during *COOH formation.[6]

The facile PT step also cast doubt on the validity of the usual practice of treating the first ET and PT as coupled. Since the first PT experiences a small free energy change at all catalytically relevant potentials, the overpotential of CO_2 activation to *COOH will be solely determined by the first ET step irrelevant to the PT energetics.[30] As shown in Table S1, the PT step shows almost no surface charge variation, which also suggests that it is

https://doi.org/10.1021/acscatal.2c01470
ACS Catal. 2022, 12, 6606−6617

not a distinctly potential-dependent step. The full revised mechanism and how it differs from the traditional PCET mechanism is provided in Figure 4d.

Competitive Relationship of CO_2RR *vs* HER. As a major side reaction in CO_2RR, HER significantly affects the CO_2RR activity and selectivity on the TM-N-C catalyst. We therefore also explored the free energy profiles (Figure 5a) of acidic HER ($H_3O + e^- \rightarrow *H + H_2O$) at −0.16, −0.41, and −0.66 V *vs* RHE. In order to simulate the experimental pH condition (pH 6.8−7.3) in agreement with CO_2RR, we corrected the free energy derived from thermodynamic integration and the details are presented in Note S7 and Table S3. Similar to CO_2 adsorption, the reaction free energy of solvated proton adsorption ($\Delta G(*H)$) is also strongly dependent on the electrode potential, with the $\Delta G(*H)$ gradually decreasing from 0.48 to −0.88 eV as the potential shifts from −0.16 to −0.66 V. By fitting a linear scaling relationship, the slope is calculated to be 2.53 eV/V, which indicates a higher potential dependence than the CO_2 adsorption step (1.65 eV/V). This indicates that the role of solvation could amplify the potential dependence for the H adsorption free energy. Interestingly, we found that the configuration of deprotonated H_2O at the final state is not as usual as the previous report about the metal catalyst.[75] Specifically, a H atom, rather than an O atom, in H_2O points toward the adsorbed hydrogen (Figure 5a). This is due to the negative net charge of −0.17|e| on the adsorbed H that electrostatically attracts the H atom in H_2O with a positive partial charge. It is known that the electrode potential has a huge effect on water orientation,[76,77] which suggests that this reorientation could be influenced by potential.

Based on the scaling relationships, we could derive the theoretical onset potential by solving for the potential value at which the free energy change becomes zero (Figure 5b). As a result, the estimated onset potentials (U_{onset}) of CO_2RR and HER are −0.22 and −0.49 V, respectively. Specifically, we could conclude that the U_{onset} of HER corresponds to the potential at which the system exhibits the highest CO Faraday efficiency (FE_{CO}) because afterwards, the competing proton adsorption would consume the electrons, block the active sites, and hence reduce the partial current density of CO_2RR. It is worth noting that our conclusions are consistent with many previous experimental observations about the CO_2RR catalyzed by Fe−N−C, where the U_{onset} of CO_2RR is around −0.2 to −0.4 V *vs* RHE and the potential of maximal FE_{CO} is approximately at −0.47 to −0.60 V *vs* RHE (see the experimental data on Table S4).[35,46,53,54,78] Conversely, the static DFT calculation results based on the traditional computational hydrogen electrode (CHE) model reached an incorrect estimation about the selectivity of CO_2RR/HER, i.e., HER would be prior to CO_2RR since the proton adsorption is more thermodynamically favorable (by 180 meV) than the *COOH formation on the Fe-N_4-C catalyst (Figure S18).

Furthermore, we observe a crossover potential (U_{cross}) between the two scaling lines in the $\Delta G-U$ curve in Figure 5b, where the $\Delta G(*CO_2^-)$ is equal to $\Delta G(*H)$. At U_{cross}, the same values of ΔG suggest the equivalent coverage of $*CO_2^-$ ($\theta_{*CO_2^-}$) and *H (θ_{*H}) on the active sites and thus the similar FE for CO production and H_2 production (see the SI for details). Interestingly, the U_{cross} is predicted to be −0.99 V, which also agrees with previous experimental reports (−0.68 to −1.00 V *vs* RHE), which are plotted together in Figure 5c. Consequently, with the three critical potentials ($U_{onset}(CO_2RR)$ = −0.22 V, $U_{onset}(HER)$ = −0.49 V, U_{cross} = −0.99 V) agreeing with experimental data semiquantitatively, we could breakdown the potential dependence of CO_2RR activity and selectivity on the Fe-N_4-C catalyst into four major stages as illustrated in Figure 5d:

(I) At $U > -0.22$ V, the current density and yield (including CO and H_2) would be extremely low since neither CO_2 adsorption nor *H formation is thermodynamically favorable ($\Delta G(*CO_2^-) > 0$ and $\Delta G(*H) > 0$).

(II) At $-0.22\ V > U > -0.49$ V, the FE_{CO} would rapidly increase since the CO_2 adsorption becomes thermodynamically feasible while HER is still unfavorable ($\Delta G(*CO_2^-) < 0$ and $\Delta G(*H) > 0$).

(III) At $-0.49\ V > U > -0.99$ V, the FE_{CO} would peak and then gradually decrease due to a climbing FE_{H2} of the HER side reaction and blockage of the active sites by *H formation ($\Delta G(*H) < 0$).

(IV) At $U < -0.99$ V, the FE_{H2} would outcompete FE_{CO} due to a higher potential dependence of *H forming energetics ($\Delta G(*H) < \Delta G(*CO_2^-)$). This also indicates that the H_2 would be the major product at very negative electrode potential (or at a high overpotential).

CONCLUSIONS

By employing constrained AIMD simulation for configurational sampling combined with the thermodynamic integration method, the free energy landscape of the key activation steps of CO_2RR and HER on the Fe-N_4-C catalyst has been explored. By analyzing the charge state and geometry of the adsorbate along the reaction coordinate and by cross-checking with a molecular fragment model, we have identified the potential determining step to be the chemisorption of CO_2 to form CO_2^- where the CO_2 molecule first undergoes a vertical ET to form a linear anion and then it bends to undergo a HOMO−LUMO crossover at the TS. The TS and FS are highly polarized due to charge redistribution and are significantly stabilized by the potential-dependent solvation effect. The PT afterward is found to be quite facile and can be excluded from overpotential calculation. Likewise, the free energy profile of competing *H formation from hydronium has also been investigated considering different potentials using the same sampling methods. Based on the free energetics, we semi-quantitatively reproduced the experimental potential-dependent CO_2RR/HER selectivity from first principles. The main conclusions are listed below:

(I) The CO_2 molecule first undergoes a vertical ET to form a linear anion, and then it bends to undergo a HOMO−LUMO crossover at the TS. The TS and FS are highly polarized due to charge redistribution and are significantly stabilized by the potential-dependent solvation effect. The reaction free energy (ΔG), energy barrier ($\Delta G^{\ddagger}$), and the location of transition state (TS) are dependent on the electrode potential. The electrode potential exhibits a linear scaling relationship with ΔG and $\Delta G^{\ddagger}$, which originates in the intersection between the harmonic region of the PES of neutral CO_2 and anionic CO_2^-.

(II) Compared to the ET step, the PT step is more thermodynamically and kinetically favorable and the ΔG is insensitive to the electrode potential. Hence, the PT should neither be rate-determining nor potential-determining in the CO_2RR process, and it should be considered to be decoupled from the ET to avoid incorrect estimation of the overpotential by including the

https://doi.org/10.1021/acscatal.2c01470
ACS Catal. 2022, 12, 6606−6617

potential-irrelevant thermodynamic contribution of the PT step

(III) The onset potential (U_{onset}) of CO_2RR, the potential at the maximal CO Faraday efficiency (FE), and the potential at $FE_{CO} = FE_{H2}$ (U_{cross}) could be determined on the basis of the theoretically derived $\Delta G-U$ linear scaling relationships, and the results are semi-quantitatively consistent with experimental data.

In a word, our study reveals the decoupled nature of the electron and proton transfer in the CO_2 activation step and scaling relationships whose potential dependence vary for different reaction intermediates. The ET−PT mechanism may occur to the electrocatalytic hydrogenation of aldehyde/ketone C═O in the area of electrosynthesis and oxygenated hydrocarbon conversion.[79,80] The proposed constrained AIMD-TI method combined with fully explicit solvation and the potential-dependent scaling relationships derived from the obtained free energy profile could be generalized to determine the thermodynamic/kinetic properties of other electrochemical reactions on similar catalyst systems and provide precise insights in line with experimental observations.

■ ASSOCIATED CONTENT

Supporting Information

The Supporting Information is available free of charge at https://pubs.acs.org/doi/10.1021/acscatal.2c01470.

Additional computational method, charge transfer analysis for the ET step, hybrid functional calculation on molecular fragments for understanding CO_2 activation chemistry, judgment of hydrogen bond formation between $*CO_2^-$ and solvation environment, proton-transfer step, DFT calculations based on the computational hydrogen electrode (CHE) model, pH effect and theoretical implication of U_{cross}, pros and cons of the constant-charge AIMD-TI *vs* constant-potential methods and the effect of electrolyte and ionic additives, input file and coordinates for structural model (PDF)

■ AUTHOR INFORMATION

Corresponding Author

Yang-Gang Wang − *Shenzhen Key Laboratory of Energy Chemistry, Southern University of Science and Technology, Shenzhen 518055, China; Department of Chemistry and Guangdong Provincial Key Laboratory of Catalysis, Southern University of Science and Technology, Shenzhen, Guangdong 518055, China;* orcid.org/0000-0002-0582-0855; Email: wangyg@sustech.edu.cn

Authors

Hao Cao − *Shenzhen Key Laboratory of Energy Chemistry, Southern University of Science and Technology, Shenzhen 518055, China; Department of Chemistry and Guangdong Provincial Key Laboratory of Catalysis, Southern University of Science and Technology, Shenzhen, Guangdong 518055, China*

Zisheng Zhang − *Department of Chemistry and Biochemistry, University of California, Los Angeles, California 90095, United States;* orcid.org/0000-0002-4370-4038

Jie-Wei Chen − *Shenzhen Key Laboratory of Energy Chemistry, Southern University of Science and Technology, Shenzhen 518055, China; Department of Chemistry and Guangdong Provincial Key Laboratory of Catalysis, Southern University of Science and Technology, Shenzhen, Guangdong 518055, China*

Complete contact information is available at: https://pubs.acs.org/10.1021/acscatal.2c01470

Author Contributions

#H. C. and Z. Z. contributed equally to this paper.

Notes

The authors declare no competing financial interest.

■ ACKNOWLEDGMENTS

This work was financially supported by NSFC (No. 22022504) of China, Guangdong "Pearl River" Talent Plan (No. 2019QN01L353), Higher Education Innovation Strong School Project of Guangdong Province of China (2020KTSCX122), Guangdong Provincial Key Laboratory of Catalysis (No. 2020B121201002), and the Shenzhen Science and Technology Innovation Committee (Grant No. ZDSYS20200421111001787). The computational resources were also supported by the Center for Computational Science and Engineering at the Southern University of Science and Technology (SUSTech) and the CHEM high-performance computing cluster (CHEM-HPC) located at the Department of Chemistry, SUSTech.

■ REFERENCES

(1) Jin, S.; Hao, Z.; Zhang, K.; Yan, Z.; Chen, J. Advances and Challenges for the Electrochemical Reduction of CO_2 to CO: From Fundamentals to Industrialization. *Angew. Chem., Int. Ed.* **2021**, *60*, 20627−20648.

(2) Nielsen, D. U.; Hu, X. M.; Daasbjerg, K.; Skrydstrup, T. Chemically and Electrochemically Catalysed Conversion of CO_2 to CO with Follow-up Utilization to Value-Added Chemicals. *Nat. Catal.* **2018**, *1*, 244−254.

(3) Wagner, A.; Sahm, C. D.; Reisner, E. Towards Molecular Understanding of Local Chemical Environment Effects in Electro- and Photocatalytic CO_2 Reduction. *Nat. Catal.* **2020**, *3*, 775−786.

(4) Birdja, Y. Y.; Pérez-Gallent, E.; Figueiredo, M. C.; Göttle, A. J.; Calle-Vallejo, F.; Koper, M. T. M. Advances and Challenges in Understanding the Electrocatalytic Conversion of Carbon Dioxide to Fuels. *Nat. Energy* **2019**, *4*, 732−745.

(5) Liu, C.; Wu, Y.; Sun, K.; Fang, J.; Huang, A.; Pan, Y.; Cheong, W.-C.; Zhuang, Z.; Zhuang, Z.; Yuan, Q.; Xin, H. L.; Zhang, C.; Zhang, J.; Xiao, H.; Chen, C.; Li, Y. Constructing FeN4/Graphitic Nitrogen Atomic Interface for High-Efficiency Electrochemical CO_2 Reduction over a Broad Potential Window. *Chem* **2021**, 1297−1307.

(6) Gu, J.; Hsu, C.-S.; Bai, L.; Chen, H. M.; Hu, X. Atomically Dispersed Fe^{3+} Sites Catalyze Efficient CO_2 Electroreduction to CO. *Science* **2019**, *364*, 1091−1094.

(7) Wang, Y.; Wang, M.; Zhang, Z.; Wang, Q.; Jiang, Z.; Lucero, M.; Zhang, X.; Li, X.; Gu, M.; Feng, Z.; Liang, Y. Phthalocyanine Precursors To Construct Atomically Dispersed Iron Electrocatalysts. *ACS Catal.* **2019**, *9*, 6252−6261.

(8) Zhang, X.; Wu, Z.; Zhang, X.; Li, L.; Li, Y.; Xu, H.; Li, X.; Yu, X.; Zhang, Z.; Liang, Y.; Wang, H. Highly Selective and Active CO_2 Reduction Electrocatalysts Based on Cobalt Phthalocyanine/Carbon Nanotube Hybrid Structures. *Nat. Commun.* **2017**, *8*, 14675.

(9) Jiang, K.; Siahrostami, S.; Zheng, T.; Hu, Y.; Hwang, S.; Stavitski, E.; Peng, Y.; Dynes, J.; Gangisetty, M.; Su, D.; Attenkofer, K.; Wang, H. Isolated Ni Single Atoms in Graphene Nanosheets for High-Performance CO_2 Reduction. *Energy Environ. Sci.* **2018**, *11*, 893−903.

(10) Yang, H. B.; Hung, S. F.; Liu, S.; Yuan, K.; Miao, S.; Zhang, L.; Huang, X.; Wang, H. Y.; Cai, W.; Chen, R.; Gao, J.; Yang, X.; Chen, W.; Huang, Y.; Chen, H. M.; Li, C. M.; Zhang, T.; Liu, B. Atomically Dispersed Ni(i) as the Active Site for Electrochemical CO_2 Reduction. *Nat. Energy* **2018**, *3*, 140−147.

(11) Zhang, X.; Wang, Y.; Gu, M.; Wang, M.; Zhang, Z.; Pan, W.; Jiang, Z.; Zheng, H.; Lucero, M.; Wang, H.; Sterbinsky, G. E.; Ma, Q.; Wang, Y. G.; Feng, Z.; Li, J.; Dai, H.; Liang, Y. Molecular Engineering of Dispersed Nickel Phthalocyanines on Carbon Nanotubes for Selective CO_2 Reduction. *Nat. Energy* **2020**, *5*, 684−692.
(12) Franco, F.; Rettenmaier, C.; Jeon, H. S.; Cuenya, B. R. Transition Metal-Based Catalysts for the Electrochemical CO_2 reduction: From Atoms and Molecules to Nanostructured Materials. *Chem. Soc. Rev.* **2020**, *49*, 6884−6946.
(13) Chia, X.; Pumera, M. Characteristics and Performance of Two-Dimensional Materials for Electrocatalysis. *Nat. Catal.* **2018**, *1*, 909−921.
(14) Nguyen, D. L. T.; Kim, Y.; Hwang, Y. J.; Won, D. H. Progress in Development of Electrocatalyst for CO_2 Conversion to Selective CO Production. *Carbon Energy* **2020**, *2*, 72−98.
(15) Vijay, S.; Gauthier, J. A.; Heenen, H. H.; Bukas, V. J.; Kristoffersen, H. H.; Chan, K. Dipole-Field Interactions Determine the CO_2Reduction Activity of 2D Fe-N-C Single-Atom Catalysts. *ACS Catal.* **2020**, *10*, 7826−7835.
(16) Bagger, A.; Ju, W.; Varela, A. S.; Strasser, P.; Rossmeisl, J. Single Site Porphyrine-like Structures Advantages over Metals for Selective Electrochemical CO_2 Reduction. *Catal. Today* **2017**, *288*, 74−78.
(17) Li, X.; Bi, W.; Chen, M.; Sun, Y.; Ju, H.; Yan, W.; Zhu, J.; Wu, X.; Chu, W.; Wu, C.; Xie, Y. Exclusive Ni-N_4 Sites Realize Near-Unity CO Selectivity for Electrochemical CO_2 Reduction. *J. Am. Chem. Soc.* **2017**, *139*, 14889−14892.
(18) Magnussen, O. M.; Groß, A. Toward an Atomic-Scale Understanding of Electrochemical Interface Structure and Dynamics. *J. Am. Chem. Soc.* **2019**, *141*, 4777−4790.
(19) Björneholm, O.; Hansen, M. H.; Hodgson, A.; Liu, L. M.; Limmer, D. T.; Michaelides, A.; Pedevilla, P.; Rossmeisl, J.; Shen, H.; Tocci, G.; Tyrode, E.; Walz, M. M.; Werner, J.; Bluhm, H. Water at Interfaces. *Chem. Rev.* **2016**, *116*, 7698−7726.
(20) Gauthier, J. A.; Fields, M.; Bajdich, M.; Chen, L. D.; Sandberg, R. B.; Chan, K.; Nørskov, J. K. Facile Electron Transfer to CO_2 during Adsorption at the Metal|Solution Interface. *J. Phys. Chem. C* **2019**, *123*, 29278−29283.
(21) Chernyshova, I. V.; Ponnurangam, S. Activation of CO_2 at the Electrode-Electrolyte Interface by a Co-Adsorbed Cation and an Electric Field. *Phys. Chem. Chem. Phys.* **2019**, *21*, 8797−8807.
(22) Lee, J. H.; Kattel, S.; Xie, Z.; Tackett, B. M.; Wang, J.; Liu, C. J.; Chen, J. G. Understanding the Role of Functional Groups in Polymeric Binder for Electrochemical Carbon Dioxide Reduction on Gold Nanoparticles. *Adv. Funct. Mater.* **2018**, *28*, 1804762.
(23) Nørskov, J. K.; Rossmeisl, J.; Logadottir, A.; Lindqvist, L.; Kitchin, J. R.; Bligaard, T.; Jónsson, H. Origin of the Overpotential for Oxygen Reduction at a Fuel-Cell Cathode. *J. Phys. Chem. B* **2004**, *108*, 17886−17892.
(24) Tripkovic, V.; Vanin, M.; Karamad, M.; Björketun, M. E.; Jacobsen, K. W.; Thygesen, K. S.; Rossmeisl, J. Electrochemical CO_2 and CO Reduction on Metal-Functionalized Porphyrin-like Graphene. *J. Phys. Chem. C* **2013**, *117*, 9187−9195.
(25) Cheng, M. J.; Kwon, Y.; Head-Gordon, M.; Bell, A. T. Tailoring Metal-Porphyrin-Like Active Sites on Graphene to Improve the Efficiency and Selectivity of Electrochemical CO_2 Reduction. *J. Phys. Chem. C* **2015**, *119*, 21345−21352.
(26) Siahrostami, S.; Jiang, K.; Karamad, M.; Chan, K.; Wang, H.; Nørskov, J. Theoretical Investigations into Defected Graphene for Electrochemical Reduction of CO_2. *ACS Sustainable Chem. Eng.* **2017**, *5*, 11080−11085.
(27) Göttle, A. J.; Koper, M. T. M. Proton-Coupled Electron Transfer in the Electrocatalysis of CO_2 Reduction: Prediction of Sequential vs. Concerted Pathways Using DFT. *Chem. Sci.* **2016**, *8*, 458−465.
(28) Hammes-Schiffer, S. Introduction: Proton-Coupled Electron Transfer. *Chem. Rev.* **2010**, *110*, 6937−6938.
(29) Solis, B. H.; Hammes-Schiffer, S. Proton-Coupled Electron Transfer in Molecular Electrocatalysis: Theoretical Methods and Design Principles. *Inorg. Chem.* **2014**, *53*, 6427−6443.
(30) Tyburski, R.; Liu, T.; Glover, S. D.; Hammarström, L. Proton-Coupled Electron Transfer Guidelines, Fair and Square. *J. Am. Chem. Soc.* **2021**, *143*, 560−576.
(31) Varela, A. S.; Kroschel, M.; Leonard, N. D.; Ju, W.; Steinberg, J.; Bagger, A.; Rossmeisl, J.; Strasser, P. PH Effects on the Selectivity of the Electrocatalytic CO_2 Reduction on Graphene-Embedded Fe-N-C Motifs: Bridging Concepts between Molecular Homogeneous and Solid-State Heterogeneous Catalysis. *ACS Energy Lett.* **2018**, *3*, 812−817.
(32) Zhao, K.; Nie, X.; Wang, H.; Chen, S.; Quan, X.; Yu, H.; Choi, W.; Zhang, G.; Kim, B.; Chen, J. G. Selective Electroreduction of CO_2 to Acetone by Single Copper Atoms Anchored on N-Doped Porous Carbon. *Nat. Commun.* **2020**, *11*, 2455.
(33) Liu, S.; Cheng, L.; Li, K.; Yin, C.; Tang, H.; Wang, Y.; Wu, Z. RuN4 Doped Graphene Oxide, a Highly Efficient Bifunctional Catalyst for Oxygen Reduction and CO_2 Reduction from Computational Study. *ACS Sustainable Chem. Eng.* **2019**, *7*, 8136−8144.
(34) Zhang, H.; Li, J.; Xi, S.; Du, Y.; Hai, X.; Wang, J.; Xu, H.; Wu, G.; Zhang, J.; Lu, J.; Wang, J. A Graphene-Supported Single-Atom FeN_5 Catalytic Site for Efficient Electrochemical CO_2 Reduction. *Angew. Chem., Int. Ed.* **2019**, *58*, 14871−14876.
(35) Qin, X.; Zhu, S.; Xiao, F.; Zhang, L.; Shao, M. Active Sites on Heterogeneous Single-Iron-Atom Electrocatalysts in CO_2 Reduction Reaction. *ACS Energy Lett.* **2019**, *4*, 1778−1783.
(36) Möller, T.; Ju, W.; Bagger, A.; Wang, X.; Luo, F.; Ngo Thanh, T.; Varela, A. S.; Rossmeisl, J.; Strasser, P. Efficient CO_2 to CO Electrolysis on Solid Ni-N-C Catalysts at Industrial Current Densities. *Energy Environ. Sci.* **2019**, *12*, 640−647.
(37) Yang, F.; Song, P.; Liu, X.; Mei, B.; Xing, W.; Jiang, Z.; Gu, L.; Xu, W. Highly Efficient CO_2 Electroreduction on ZnN_4-Based Single-Atom Catalyst. *Angew. Chem., Int. Ed.* **2018**, *57*, 12303−12307.
(38) Pan, F.; Zhang, H.; Liu, K.; Cullen, D.; More, K.; Wang, M.; Feng, Z.; Wang, G.; Wu, G.; Li, Y. Unveiling Active Sites of CO_2 Reduction on Nitrogen-Coordinated and Atomically Dispersed Iron and Cobalt Catalysts. *ACS Catal.* **2018**, *8*, 3116−3122.
(39) Zhao, X.; Liu, Y. Unveiling the Active Structure of Single Nickel Atom Catalysis: Critical Roles of Charge Capacity and Hydrogen Bonding. *J. Am. Chem. Soc.* **2020**, *142*, 5773−5777.
(40) Li, J.; Liu, J.; Yang, B. Insights into the Adsorption/Desorption of CO_2 and CO on Single-Atom Fe-Nitrogen-Graphene Catalyst under Electrochemical Environment. *J. Energy Chem.* **2020**, *53*, 20−25.
(41) Long, J.; Guo, C.; Fu, X.; Jing, H.; Qin, G.; Li, H.; Xiao, J. Unveiling Potential Dependence in NO Electroreduction to Ammonia. *J. Phys. Chem. Lett.* **2021**, *12*, 6988−6995.
(42) Choi, C.; Gu, G. H.; Noh, J.; Park, H. S.; Jung, Y. Understanding Potential-Dependent Competition between Electrocatalytic Dinitrogen and Proton Reduction Reactions. *Nat. Commun.* **2021**, *12*, 4353.
(43) Shen, J.; Kortlever, R.; Kas, R.; Birdja, Y. Y.; Diaz-Morales, O.; Kwon, Y.; Ledezma-Yanez, I.; Schouten, K. J. P.; Mul, G.; Koper, M. T. M. Electrocatalytic Reduction of Carbon Dioxide to Carbon Monoxide and Methane at an Immobilized Cobalt Protoporphyrin. *Nat. Commun.* **2015**, *6*, 8177.
(44) Singh, M. R.; Kwon, Y.; Lum, Y.; Ager, J. W., III; Bell, A. T. Hydrolysis of Electrolyte Cations Enhances the Electrochemical Reduction of CO_2 over Ag and Cu. *J. Am. Chem. Soc.* **2016**, *138*, 13006−13012.
(45) Goyal, A.; Marcandalli, G.; Mints, V. A.; Koper, M. T. M. Competition between CO_2 Reduction and Hydrogen Evolution on a Gold Electrode under Well-Defined Mass Transport Conditions. *J. Am. Chem. Soc.* **2020**, *142*, 4154−4161.
(46) Ju, W.; Bagger, A.; Hao, G.-P.; Varela, A. S.; Sinev, I.; Bon, V.; Cuenya, B. R.; Kaskel, S.; Rossmeisl, J.; Strasser, P. Understanding Activity and Selectivity of Metal-Nitrogen-Doped Carbon Catalysts for Electrochemical Reduction of CO_2. *Nat. Commun.* **2017**, *8*, 944.
(47) Le, J.-B.; Yang, X.-H.; Zhuang, Y.-B.; Jia, M.; Cheng, J. Recent Progress toward Ab Initio Modeling of Electrocatalysis. *J. Phys. Chem. Lett.* **2021**, *12*, 8924−8931.

https://doi.org/10.1021/acscatal.2c01470
ACS Catal. 2022, 12, 6606−6617

(48) Sakong, S.; Groß, A. The Electric Double Layer at Metal-Water Interfaces Revisited Based on a Charge Polarization Scheme. *J. Chem. Phys.* **2018**, *149*, 84705.
(49) Pedroza, L. S.; Poissier, A.; Fernández-Serra, M. V. Local Order of Liquid Water at Metallic Electrode Surfaces. *J. Chem. Phys.* **2015**, *142*, 34706.
(50) Chen, J.-W.; Zhang, Z.; Yan, H.-M.; Xia, G.-J.; Cao, H.; Wang, Y.-G. Pseudo-Adsorption and Long-Range Redox Coupling during Oxygen Reduction Reaction on Single Atom Electrocatalyst. *Nat. Commun.* **2022**, *13*, 1734.
(51) Wikfeldt, K. T.; Leetmaa, M.; Ljungberg, M. P.; Nilsson, A.; Pettersson, L. G. M. On the Range of Water Structure Models Compatible with X-Ray and Neutron Diffraction Data. *J. Phys. Chem. B* **2009**, *113*, 6246−6255.
(52) Klug, C. M.; Cardenas, A. J. P.; Bullock, R. M.; O'Hagan, M.; Wiedner, E. S. Reversing the Tradeoff between Rate and Overpotential in Molecular Electrocatalysts for H_2 Production. *ACS Catal.* **2018**, *8*, 3286−3296.
(53) Hu, X. M.; Hval, H. H.; Bjerglund, E. T.; Dalgaard, K. J.; Madsen, M. R.; Pohl, M. M.; Welter, E.; Lamagni, P.; Buhl, K. B.; Bremholm, M.; Beller, M.; Pedersen, S. U.; Skrydstrup, T.; Daasbjerg, K. Selective CO_2 Reduction to CO in Water Using Earth-Abundant Metal and Nitrogen-Doped Carbon Electrocatalysts. *ACS Catal.* **2018**, *8*, 6255−6264.
(54) Li, X.; Xi, S.; Sun, L.; Dou, S.; Huang, Z.; Su, T.; Wang, X. Isolated FeN_4 Sites for Efficient Electrocatalytic CO_2 Reduction. *Adv. Sci.* **2020**, *7*, 2001545.
(55) Zhao, X.; Liu, Y. Origin of Selective Production of Hydrogen Peroxide by Electrochemical Oxygen Reduction. *J. Am. Chem. Soc.* **2021**, *143*, 9423−9428.
(56) Vandevondele, J.; Krack, M.; Mohamed, F.; Parrinello, M.; Chassaing, T.; Hutter, J. Quickstep: Fast and Accurate Density Functional Calculations Using a Mixed Gaussian and Plane Waves Approach. *Comput. Phys. Commun.* **2005**, *167*, 103−128.
(57) Perdew, J. P.; Burke, K.; Ernzerhof, M. Generalized Gradient Approximation Made Simple. *Phys. Rev. Lett.* **1996**, *77*, 3865−3868.
(58) Martyna, G. J.; Klein, M. L.; Tuckerman, M. Nosé-Hoover Chains: The Canonical Ensemble via Continuous Dynamics. *J. Chem. Phys.* **1992**, *97*, 2635−2643.
(59) Hoover, W. G. Canonical Dynamics: Equilibrium Phase-Space Distributions. *Phys. Rev. A* **1985**, *31*, 1695−1697.
(60) Grimme, S.; Antony, J.; Ehrlich, S.; Krieg, H. A Consistent and Accurate Ab Initio Parametrization of Density Functional Dispersion Correction (DFT-D) for the 94 Elements H-Pu. *J. Chem. Phys.* **2010**, *132*, 154104.
(61) Grimme, S.; Ehrlich, S.; Goerigk, L. Effect of the Damping Function in Dispersion Corrected Density Functional Theory. *J. Comput. Chem.* **2011**, *32*, 1456−1465.
(62) Carter, E. A.; Ciccotti, G.; Hynes, J. T.; Kapral, R. Constrained Reaction Coordinate Dynamics for the Simulation of Rare Events. *Chem. Phys. Lett.* **1989**, *156*, 472−477.
(63) Sprik, M.; Ciccotti, G. Free Energy from Constrained Molecular Dynamics. *J. Chem. Phys.* **1998**, *109*, 7737−7744.
(64) Granda-Marulanda, L. P.; Rendón-Calle, A.; Builes, S.; Illas, F.; Koper, M. T. M.; Calle-Vallejo, F. A Semiempirical Method to Detect and Correct DFT-Based Gas-Phase Errors and Its Application in Electrocatalysis. *ACS Catal.* **2020**, *10*, 6900−6907.
(65) Yu, M.; Trinkle, D. R. Accurate and Efficient Algorithm for Bader Charge Integration. *J. Chem. Phys.* **2011**, *134*, 064111.
(66) Chen, J.; Li, C.; Shi, G. Graphene Materials for Electrochemical Capacitors. *J. Phys. Chem. Lett.* **2013**, *4*, 1244−1253.
(67) Choi, C. H.; Lim, H. K.; Chung, M. W.; Chon, G.; Ranjbar Sahraie, N.; Altin, A.; Sougrati, M. T.; Stievano, L.; Oh, H. S.; Park, E. S.; Luo, F.; Strasser, P.; Dražić, G.; Mayrhofer, K. J. J.; Kim, H.; Jaouen, F. The Achilles' Heel of Iron-Based Catalysts during Oxygen Reduction in an Acidic Medium. *Energy Environ. Sci.* **2018**, *11*, 3176−3182.
(68) Cheng, T.; Xiao, H.; Goddard, W. A. Full Atomistic Reaction Mechanism with Kinetics for CO Reduction on Cu(100) from Ab Initio Molecular Dynamics Free-Energy Calculations at 298 K. *Proc. Natl. Acad. Sci. U. S. A.* **2017**, *114*, 1795−1800.
(69) Abidi, N.; Bonduelle-Skrzypczak, A.; Steinmann, S. N. Revisiting the Active Sites at the MoS_2/H_2O Interface via Grand-Canonical DFT: The Role of Water Dissociation. *ACS Appl. Mater. Interfaces* **2020**, *12*, 31401−31410.
(70) Frisch, M. J.; Trucks, G. W.; Schlegel, H. B.; Scuseria, G. E.; Robb, M. A.; Cheeseman, J. R.; Scalmani, G.; Barone, V.; Petersson, G. A.; Nakatsuji, H. *Gaussian 16*; Gaussian, Inc.: Wallingford, CT 2016.
(71) Adamo, C.; Barone, V. Toward Reliable Density Functional Methods without Adjustable Parameters: The PBE0 Model. *J. Chem. Phys.* **1999**, *110*, 6158−6170.
(72) Weigend, F.; Ahlrichs, R. Balanced Basis Sets of Split Valence, Triple Zeta Valence and Quadruple Zeta Valence Quality for H to Rn: Design and Assessment of Accuracy. *Phys. Chem. Chem. Phys.* **2005**, *7*, 3297−3305.
(73) Lu, T.; Chen, F. Multiwfn: A Multifunctional Wavefunction Analyzer. *J. Comput. Chem.* **2012**, *33*, 580−592.
(74) Ju, W.; Bagger, A.; Wang, X.; Tsai, Y.; Luo, F.; Möller, T.; Wang, H.; Rossmeisl, J.; Varela, A. S.; Strasser, P. Unraveling Mechanistic Reaction Pathways of the Electrochemical CO_2 Reduction on Fe-N-C Single-Site Catalysts. *ACS Energy Lett.* **2019**, *4*, 1663−1671.
(75) Kronberg, R.; Laasonen, K. Reconciling the Experimental and Computational Hydrogen Evolution Activities of Pt(111) through DFT-Based Constrained MD Simulations. *ACS Catal.* **2021**, *11*, 8062−8078.
(76) Le, J.-B.; Fan, Q.-Y.; Li, J.-Q.; Cheng, J. Molecular Origin of Negative Component of Helmholtz Capacitance at Electrified Pt(111)/Water Interface. *Sci. Adv.* **2020**, *6*, No. eabb1219.
(77) Le, J.; Iannuzzi, M.; Cuesta, A.; Cheng, J. Determining Potentials of Zero Charge of Metal Electrodes versus the Standard Hydrogen Electrode from Density-Functional-Theory-Based Molecular Dynamics. *Phys. Rev. Lett.* **2017**, *119*, No. 016801.
(78) Huan, T. N.; Ranjbar, N.; Rousse, G.; Sougrati, M.; Zitolo, A.; Mougel, V.; Jaouen, F.; Fontecave, M. Electrochemical Reduction of CO_2 Catalyzed by Fe-N-C Materials: A Structure-Selectivity Study. *ACS Catal.* **2017**, *7*, 1520−1525.
(79) Cantu, D. C.; Padmaperuma, A. B.; Nguyen, M.-T.; Akhade, S. A.; Yoon, Y.; Wang, Y.-G.; Lee, M.-S.; Glezakou, V.-A.; Rousseau, R.; Lilga, M. A. A Combined Experimental and Theoretical Study on the Activity and Selectivity of the Electrocatalytic Hydrogenation of Aldehydes. *ACS Catal.* **2018**, *8*, 7645−7658.
(80) Du, L.; Shao, Y.; Sun, J.; Yin, G.; Du, C.; Wang, Y. Electrocatalytic Valorisation of Biomass Derived Chemicals. *Catal. Sci. Technol.* **2018**, *8*, 3216−3232.

https://doi.org/10.1021/acscatal.2c01470
ACS Catal. 2022, 12, 6606−6617